

Spectral observations of the systems with the disturbed spiral arms: Arp 42, Arp 82 and Arp 58

Anatoly V. Zasov,^{1,2}★ Anna S. Saburova,¹ Oleg V. Egorov,^{1,3} Sergei N. Dodonov³

¹ Sternberg Astronomical Institute, Moscow M.V. Lomonosov State University, Universitetskij pr., 13, Moscow, 119234, Russia

² Faculty of Physics, Moscow M.V. Lomonosov State University, Leninskie gory 1, Moscow, 119991, Russia

³ Special Astrophysical Observatory, Russian Academy of Sciences, Nizhniy Arkhyz, Karachai-Cherkessian Republic, 357147, Russia

8 April 2019

ABSTRACT

We study three Arp' systems of peculiar galaxies: Arp 42 (NGC 5829), Arp 82 (NGC 2535/36) and Arp 58 (UGC 4457), using the long-slit spectral observations carried out at the 6m telescope BTA of Special Astrophysical Observatory. Arp 82 and Arp 58 are the M51-type systems. In the third system – Arp 42, there are two extremely luminous kpc-sized clumps observed at the ends of the bifurcated spiral arm, however the source of perturbations remains unknown. From the emission line measurements we analyzed the distribution of gas line-of-sight (LOS) velocity, velocity dispersion and gas-phase metallicity along the slits estimated by different methods. A special attention is paid to the young regions of star formation at the peripheries of the galaxies and in tidal debris, their connection with gas kinematics and abundance. All three systems show the signs of velocity disturbances and the presence of regions of locally enhanced gas velocity dispersion, as well as the regions of diffuse ionized gas. A distribution of oxygen reveals shallow radial abundance gradients, typical for interacting systems. A faint spiral-like branches of tidal bridges which are observed in NGC 2535 and UGC 4457 may represent the remnants of pre-existing "old" mode of spiral waves.

Key words: galaxies: kinematics and dynamics, galaxies: evolution

1 INTRODUCTION

Tidal interactions of spatially close gas-rich galaxies affect mostly their gas component due to the collisional nature of gas and low dispersion of gas velocities. Some fraction of gas of interacting galaxies loses angular momentum and moves closer to the center, usually stimulating a burst of star formation, while some gas and stars may be thrown out of galactic discs, often forming tidal streams stretching far away from parent galaxies. At the stage of strong interaction, direct collisions of gas flows can occur leading to shock-induced star formation (see e.g. Maji et al. 2017 and references therein). Formation of stars is often observed both in a far periphery of disc and in tidal debris of galaxies including a formation of gravitationally bound tidal dwarf galaxies, which takes place under favourable conditions (see the surveys by Weilbacher et al. 2002; Duc & Renaud 2013).

Mechanisms which can promote a formation of the extended star-forming regions at the periphery of galaxies and in tidal debris in low gas density conditions, as well as their subsequent evolution, is the actively debated problem (see e.g. Wetzstein et al. 2007; Bournaud 2011). Obviously, con-

crete scenarios depend on many factors, and they are different for different interacting systems. In addition to the gravitation instability of gas in tidal debris, which does not always take place, a key role in triggering star formation may play such events as a supersonic turbulence, ram pressure and interaction with the external gas (Renaud et al. 2014; Maji et al. 2017; Smith et al. 2013; Kapferer et al. 2008; Tonnesen & Bryan 2012). So, as it was noted earlier by Boquien et al. (2009), collisional debris may be considered as laboratories to study star formation.

It is essential that the galaxies we consider and their tidal structures are in the very unstable phase of evolution when stellar and gas spatial distributions and their velocities may experience a significant change over a characteristic dynamic time of about 10^8 yr which complicates the observed picture. Although strong interaction affects all regions of a galaxy, it manifests itself in different ways at different distances from the centre: due to gravity torques the gas loses angular momentum in the inner galaxy and gains it at larger radii (Bournaud 2011). As a result there is a local increase of gas density and activation of star formation in the circumnuclear region of a galaxy (Noguchi 1988; Hernquist 1989), and a decrease in gas density in other regions, which in turn may cause a flattening of radial gradient of gas abundance (Kewley et al.

★ E-mail: zasov@sai.msu.ru

2006, 2010). Gas and stars ejected from the disc may either leave the galaxy or fall backward (see, e.g. Elmegreen et al. 1993), they may form a tidal tail or tidal dwarf galaxies (Duc et al. 2000; Duc & Renaud 2013). Measuring gas velocities and radial gradients of chemical composition in interacting systems allows us to understand better the star formation conditions and the ways of the evolution of galaxies, which have experienced or experienced strong tidal disturbances in the past.

In this paper we continue to describe the results of spectral observations at the 6m telescope BTA of Special Astrophysical Observatory of disturbed galaxies with local regions of star formation in the periphery of discs or in the intergalactic space which we started in Zasov et al. (2015, 2016, 2017, 2018). Here we focus on the three Arp systems Arp 42, Arp 82, and Arp 58. The main components of these systems are the late-type star-forming spiral galaxies with peculiar spiral structures (a presence of tidal arms or arm bifurcation), evidencing their perturbed state. The galaxies are characterized by active star formation, where the numerous local sites (clumps) of emission gas and young stars are noticeable not only in their central parts, but also at the far disc periphery and in tidal debris. Composite SDSS *g,r,i*-band images of the galaxies are shown in Fig. 1.

The structure of this paper is as follows. In the next section we give the short information on the considered systems; the observation and data reduction procedures are presented in Section 3; it is followed by Section 4 describing the data analysis techniques we use; the results of observations are given in Section 5, and their discussion is presented in Section 6. Section 7 summarizes our conclusions.

2 A SHORT INFORMATION ON THE CHOSEN GALAXIES

2.1 Arp 42

Arp 42 is the poorly studied system, consisting of Sc-type galaxy NGC 5829 and the irregular-looking IC4526 observed at the projected distance of $2.3'$, or about three times of its optical radius $R_{25} = 0.7'$. R-band surface photometry of this system was carried out by Reshetnikov et al. (1993). Curiously, the satellite galaxy is most probably a background object in spite of its peculiar asymmetric shape and the extended faint outer arm looking like a tidal tail (see Fig 1). Indeed, the systemic velocities V_{GSR} of NGC 5829 and IC 4526 are 5759 km s^{-1} and 13732 km s^{-1} respectively (HYPERLEDA¹, Makarov et al. 2014), evidencing that these galaxies are not interacting ones. Since there are no other objects of comparable brightness in the vicinity, hereafter we will consider Arp 42 as a single object NGC 5829, assuming its redshift-based distance to be 78 Mpc. It is a gas-rich late-type galaxy. Its total mass of neutral hydrogen is about $2 \times 10^{10} M_{\odot}$ (Hyperleda; see also Casasola et al. 2004). Mass of stellar population may be found from r-band luminosity using the model ratio $M/L_r \approx 2.0$ (Bell et al. 2003) for the color index $(g - r) = 0.54$ corrected for Galactic extinction estimated from SDSS images. The resulting value is $M \approx 5 \times 10^{10} M_{\odot}$.

NGC 5829 is a Grand Design-type galaxy, its two arms look non-identical. The southern spiral arm contains bright clumps of H II. Remarkably, this arm contains two or three straight sections ('rows'). Such features often observed in galaxies with the ordered spiral arms may be considered as a sign of strong large-scale shock waves linked with spiral arms (see Chernin et al. 2001; Butenko & Khoperskov 2017, and the references therein). In contrast, the opposite (northern) spiral arm looks rather smoothed and badly defined, although the extended emission regions are observed along the whole arm. Its outer fraction is bifurcated, and both split components contain a similarly looking kpc-sized unusually bright compact emission regions (we'll call them BER1,2, see Fig. 1), embedded into the area of the enhanced brightness of about 6 kpc length, slightly stretched along their parent spiral branches.

2.2 Arp 82

Arp 82=VV 009 is the system of M51-type. It consists of a luminous spiral galaxy with the well defined two-armed spiral structure (NGC 2535), one arm of which connects or overlaps with the close satellite (NGC 2536). In addition, NGC 2535 possesses a long tidal tail as the continuation of the north spiral arm at the opposite side from the satellite. The systemic velocity of the main galaxy is close to 4000 km s^{-1} , so we adopt the distance 54 Mpc for this system.

Both galaxies NGC 2535/36 in the system Arp 82 are embedded in the large H I envelope evidently associated with the main galaxy. The extended gaseous disc is too large to be the result of the observed interaction, and most probably it existed before the galaxies became close (Kaufman et al. 1997). For the adopted distance a total mass of H I in the galaxy pair is $2.3 \times 10^{10} M_{\odot}$ (in agreement with single dish observations) where only a small portion of H I ($5 \times 10^8 M_{\odot}$) belongs to the satellite (Kaufman et al. 1997), however the latter overlaps with the gaseous tidal bridge extending from NGC 2535, which makes the H I mass estimation model-dependent.

A resolved kinematics of Arp 82 was studied by several authors. 2D velocity map was obtained by Kaufman et al. (1997) in H I line and by Amram et al. (1989) in H α line, using a scanning Fabry–Perot interferometer. Klimanov et al. (2002) also obtained long-slit velocity measurements for two slit position angles (59° and 163°) for NGC 2535 and its satellite. All authors indicate a strong non-circular gas motions caused by interaction and the distortion of the velocity field due to the bending of the outer disc of NGC 2535, although the rotation curve of the central disc of this galaxy (within $R \sim 20\text{--}25 \text{ arcsec}$) is fairly symmetric. The velocity field distortion and the uncertainty in evaluation of inclination angles of both galaxies does not allow to obtain a reliable dynamic estimate of their masses. Kaufman et al. (1997) also pointed out the enhanced turbulent velocities of H I all over the system (about 30 km s^{-1} along the LOS).

Numerical modeling of interacting galaxies with prograde rotation, whose masses are comparable (Howard et al. 1993) or differ by several times (Holmbeck et al. 2016; Kaufman et al. 1997) reproduces successfully the main observed features of Arp 82. Velocity field of gas also well agrees with the Klaric' model (see discussion in Kaufman et al. 1997). The model of interacting galaxies presented by Hancock et al.

¹ <http://leda.univ-lyon1.fr/>

(2007) indicates that the galaxies have experienced two close encounters, and the most recent encounter have caused the observed burst of star formation in both galaxies.

2.3 Arp 58

Arp 58 = UGC 4457 = VV 413 also belongs to the M51-type systems. Its main component is the Sc-type two-arm mildly inclined galaxy. The satellite is observed at the end of the SE-spiral arm at a distance of about one optical diameter $D_{25} \sim 1$ arcmin. The second spiral arm at the opposite side from the satellite has a faint extension which forms a thin curved tidal tail. Systemic velocity of the main galaxy is close to 11000 km s^{-1} , and the distance adopted in this paper is 147 Mpc.

UGC 4457 is very luminous galaxy: its corrected B-magnitude is $B_{tc} = 14.24$ (HYPERLEDA database), which corresponds to luminosity $6.6 \times 10^{10} L_{\odot}$ for the adopted distance. The satellite is a few tens of times fainter than the main galaxy. This small galaxy is observed at a stage of active star formation. Its inner part has an elliptical shape and demonstrates strong emission lines in its spectrum, however the dim outer regions of the companion are of irregular shape being distorted by interaction.

3 OBSERVATIONS AND DATA REDUCTION

The long-slit spectral observations of Arp 42, Arp 82 and Arp 58 were performed with the Russian 6-m telescope with SCORPIO-2 spectrograph (Afanasiev & Moiseev 2011). We give the log of observations in Table 1. For every galaxy it contains a position angle (PA) of the slit; date of observations; the total exposure time and seeing. We utilized the grism VPHG1200@540, which covers the spectral range 3600–7070 Å and has a dispersion of $0.87 \text{ Å pixel}^{-1}$. The spectral resolution is $\approx 5.2 \text{ Å}$ estimated as FWHM of night-sky emission lines. The scale along the slit was $0.36 \text{ arcsec pixel}^{-1}$, and the slit width was 1 arcsec. Slit positions are superimposed on the optical images of the galaxies in Fig. 1. Every slit was chosen to cross the bright star-forming clumps.

A procedure of data processing was described step-by-step in our earlier papers (Zasov et al. 2015, 2016, 2017, 2018). To process the data we used the IDL-based pipeline. Briefly, the data reduction consisted of the following stages: a bias subtraction and truncation of overscan regions, flat-field correction, the wavelength calibration based on the spectrum of He-Ne-Ar lamp, cosmic ray hit removal, summation of individual exposures, the night sky subtraction and flux calibration using the spectrophotometric stellar standards BD33d2642, BD28d4211, BD25d4655.

4 DATA ANALYSIS

In our spectra analysis we took into account the parameters of instrumental profile of the spectrograph resulted from the fitting of the twilight sky spectrum observed in the same observation runs. We convolved these parameters with the high-resolution PEGASE.HR (Le Borgne et al. 2004) simple stellar population models (SSP) and fitted the reduced spectra of galaxies. We performed it using the NBURSTS full

spectral fitting technique (Chilingarian et al. 2007a,b), which allows to fit the spectrum in a pixel space. In this method the parameters of the stellar populations are derived by nonlinear minimization of the quadratic difference chi-square between the observed and model spectra. We utilized the following parameters of SSP: age T (Gyr) and metallicity $[Z/H]$ (dex) of stellar population. The line-of-sight velocity distribution (LOSVD) of stars was parameterized by Gauss-Hermite series (see van der Marel & Franx 1993).

The emission spectra were obtained by subtraction of model stellar spectra from the observed ones. After that we fitted the Gaussian profiles to emission lines to estimate the velocity and velocity dispersion of ionized gas and the fluxes in the emission lines.

To increase the signal-to-noise ratio (S/N) of the spectra we used the adaptive binning in the fitting. The S/N threshold levels we specified for Arp 42, Arp 82 and Arp 58 are 15, 30 and 20 respectively. We used this binning to evaluate kinematics. To estimate the emission line fluxes and metallicities we utilized binning of 3 pixels for every spectrum. The pixels with $S/N < 3$ in emission lines were excluded from further pixel-by-pixel analysis.

In addition, we also analyzed the fluxes and intensities from a stacked spectra of several adjoining pixels corresponding to single star-forming clumps or to extended regions of fainter emission. A choice of the pixels interval to be stacked was made by eye in order to increase S/N to the values not less than 10 for bright emission lines; a typical size of such bins is close to the size of bright clumps crossed by slits, or about 10–15 arcsec for faint extended regions. The resulting estimates for these bins (shown by squares in Figures below) are close to those obtained from pixel-by-pixel analysis with much lower S/N and thus prove the reliability of the latter. For illustrative purposes we demonstrate in Fig. 2 the examples of spectra of the stacked bins with low and high S/N that we used in our estimates of metallicity (see below). The first one is the spectrum of the region with the coordinate $R \approx -80 \text{ arcsec}$ in Arp 82 ($PA = 342^\circ$), and the second one is for BER1 in Arp 42 ($PA = 30^\circ$).

To calculate a gas-phase metallicity, we use several methods of estimation of (O/H) abundances from the relative intensities of strong emission lines. They are based either on the empirical calibrations by comparison with the oxygen abundance values obtained by the T_e -method (S-method by Pilyugin & Grebel 2016, O3N2 method by Marino et al. 2013), or on the photoionization models of H II regions (Iz1 by Blanc et al. 2015 made using Levesque et al. 2010 photoionization models). In the most cases the shape of radial profiles of $12 + \log (\text{O}/\text{H})$ obtained by different methods looks rather similar, although there is a well known discrepancy between the theoretical and empirical estimates: theoretical models usually lead to higher values of abundances (see for example Kewley & Ellison 2008).

Note that the regions showing the signs of non-photoionization mechanism of the ionized gas excitation were not used for estimates of the oxygen abundance. The conclusion whether a region shows non-photoionization mechanism of excitation was made based on the position on the so-called BPT diagnostic diagrams proposed by Baldwin et al. (1981) and extended by Veilleux & Osterbrock (1987) for the $[\text{O III}]/\text{H}\beta$ vs $[\text{S II}]/\text{H}\alpha$ case. These diagrams are widely used to separate the different mechanisms of emission lines exci-

tation. Additionally, all regions with equivalent width of $H\alpha$ line $EW(H\alpha) < 3$ (according to [Lacerda et al. 2018](#)) were excluded as probably related to the diffuse ionized gas (DIG). In the mentioned paper the authors claimed that $EW(H\alpha) > 14 \text{ \AA}$ is typical for pure star-forming region. However applying another criterion to separate DIG from $H \text{ II}$ regions – based on $H\alpha$ flux ([Zhang et al. 2017](#)) – changes the results negligibly. Moreover, [Kumari et al. \(2019\)](#) showed that estimates of the metallicity made using O3N2 method doesn't suffer from the presence of the DIG. Hence our analysis based on at least this method should be reliable even if the DIG contribution in the remaining data is still significant.

5 RESULTS OF OBSERVATIONS

5.1 Arp 42

For Arp 42 we obtained two spectral cuts for two slit orientations. The slit positions are demonstrated in Fig. 1 (top panel). In the first cut ($PA_1 = 30^\circ$) the slit crosses the center of galaxy and BER1. This slit orientation differs at about 12° from the optical major axis (MA) ($PA_0 \approx 18^\circ$) (HYPERLEDA; [Nishiura et al. 2000](#)). In the second cut $PA_2 = 82^\circ$ the slit passes along the second branch of the spiral arm crossing the southern BER2.

The results of data processing are illustrated in Fig. 3 for $PA_1 = 30^\circ$ (left panel) and $PA_2 = 82^\circ$ (right panel). There we show the slit position overlaid on the composite SDSS g, r, i - band images (a) and from top to bottom the radial variation of: (b) observed emission lines fluxes; (c) LOS velocities; (d) LOS velocity dispersion for $PA = 30^\circ$ (e) flux ratios and (f) oxygen abundance. Circles correspond to the different emission lines. For convenience we mark the estimates having large uncertainties relative to other points at a given plot by pale-colored symbols. Stars in Fig. 3 demonstrate the stellar kinematical data obtained from the absorption spectra. Square symbols show the values obtained after stacking of several adjoining pixels corresponding to single star-forming clumps or to extended regions of fainter emission (see Section 4). For reference we mark the position of some morphological features ($H \text{ II}$ clumps, galaxies centres etc.) by vertical dotted lines. Note that for $PA = 82^\circ$ we managed to estimate only the upper limit of LOS velocity dispersion in all emission lines (50 km s^{-1}), so we do not reproduce it in the Figure.

LOS velocity profile along $PA_1 = 30^\circ$ in general agrees with that obtained earlier by [Nishiura et al. \(2000\)](#) along major axis, although it extends to larger radial distances R and is more detailed. Its shape in general reflects the shape of the rotation curve: it grows in the inner few kpc and then flattens at larger R . Local non-circular motions with the amplitude up to several tens of km s^{-1} are observed where the slit crosses bright emission regions.

Velocity dispersion of emission gas does not exceed 50 km s^{-1} , which is normal for galaxies with moderate star formation rate (here and below in this paper we provide the velocity and velocity dispersion estimates only for the regions with $S/N > 15$). Stellar velocity dispersion $c_* \sim 80\text{--}100 \text{ km s}^{-1}$ was measured only for the central part of the galaxy. This value is quite normal for late-type galaxies of similar lu-

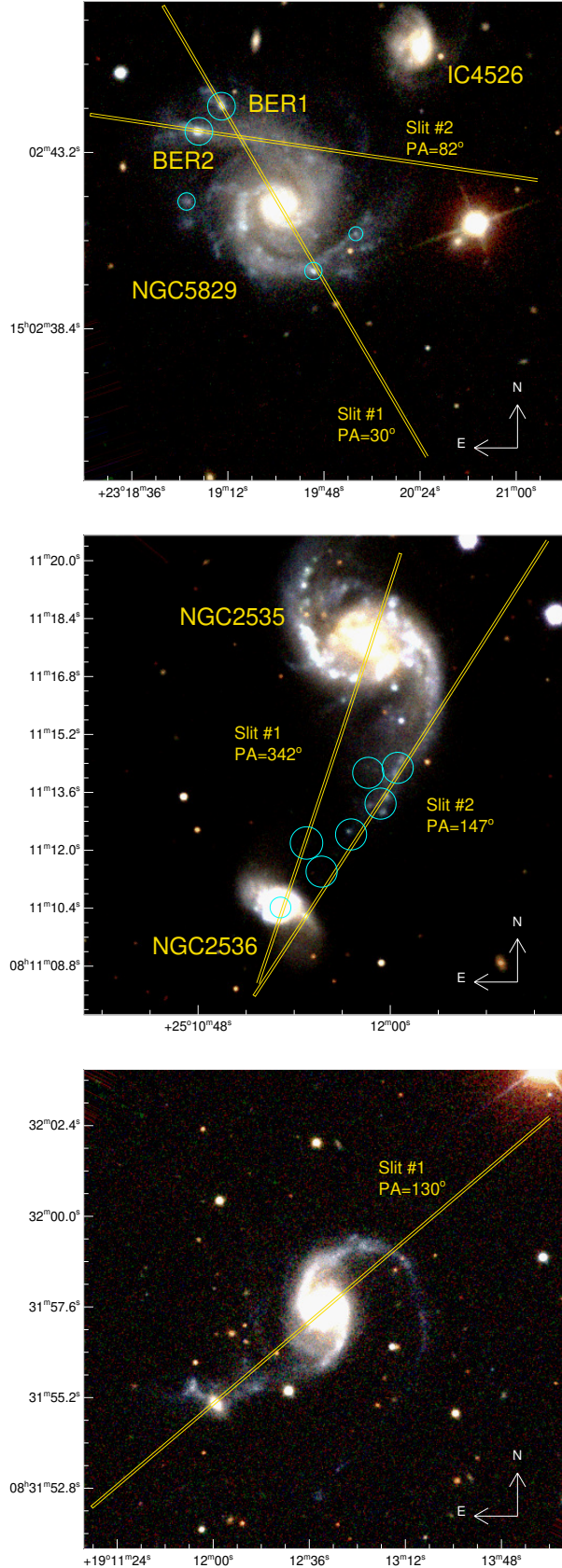


Figure 1. The positions of the slit used for spectroscopic observations overlaid on the composite SDSS g, r, i - band images of Arp 42, Arp 82, Arp 58 (from top to bottom). The circles on the images of Arp 42 and Arp 82 mark the positions of sites of star formation that were considered in the two-coloured diagrams (see below).

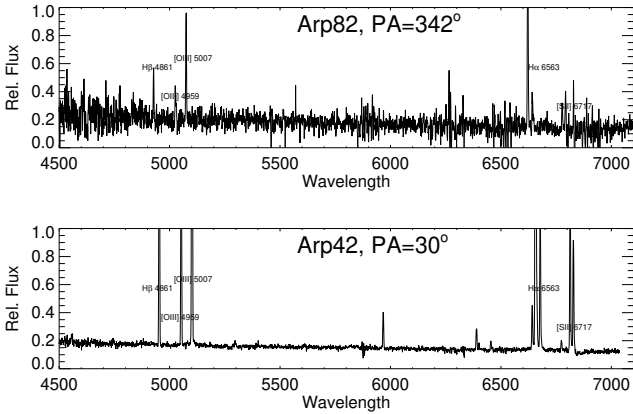


Figure 2. The examples of stacked spectra of the low (top panel) and high (bottom panel) S/N bins used for the metallicity estimate at $R \approx -80$ arcsec for Arp 82 and BER1 for Arp 42 respectively.

Table 1. Log of observations

	Slit PA ($^{\circ}$)	Date	Exposure time (s)	Seeing (arcsec)
Arp 42	30	07.04.2016	1800	1.5
Arp 42	82	24.04.2015	4500	3.3
Arp 82	342	12.12.2015	7200	4.0
Arp 82	147	13.12.2015	6300	4.0
Arp 58	130	12.12.2015	5400	1.4

minisities with moderate bulge (e.g. NGC 1084, NGC 4254, see the HYPERLEDA database (Makarov et al. 2014)).

In Fig. 4 we demonstrate the position of the emission regions crossed by the slit in the BPT diagnostic diagram, where the black ‘maximum starburst line’ (Kewley et al. 2001) separates the photoionized H II-regions from all other types of gas excitation (AGN, shocks etc.). A composite mechanism of excitation is expected for points between the black line and the gray line proposed by Kauffmann et al. (2003) (see left panel). One can see that most of the dots for Arp 42 lie in the pure photoionization region of the diagram. Several points beyond the borderlines for photoionized gas belong to regions of low surface brightness in the strong emission lines, evidencing the significant input of non-photoionizing mechanism of gas excitation.

Oxygen abundance that we found by different methods (see Fig. 3, bottom panels) shows a wide spread of values along $PA=30^{\circ}$. The empirical O3N2 and theoretical [Z] methods give higher values for the centre of the galaxy. At the same time at the effective radius of the disc $r_e = 10.8$ kpc our metallicity estimate is close to that found in the CALIFA survey (Sánchez-Menguiano et al. 2016) for NGC 5829 ($\log(O/H) = 8.43 \pm 0.05$). For the second cut, which crosses the periphery of NGC 5829, the metallicity remains roughly constant $12 + \log(O/H) \approx 8.4$. Oxygen abundance does not show any change when the slit passes through the BER1 and BER2.

5.2 Arp 82

We fulfilled two spectral cuts of Arp 82 (see Fig. 1, central panel). Slit $PA=342^{\circ}$ passes through the centres of galaxies. This orientation is close to $(PA)_0 \approx 153^{\circ}$ of major axis (MA) for the outer elliptical optical isophotes of the galaxy as well as for the kinematic MA (Kaufman et al. 1997). The second slit $PA=147^{\circ}$ runs along the bridge between the galaxies and cuts the western part of NGC 2536. The slit $PA=147^{\circ}$ also crosses the region of splitting of the spiral arm of NGC 2535 about half-way between galaxies, clearly visible in GALEX image (see Section 6).

Profiles of LOS velocities, velocity dispersion, line intensities and oxygen abundance are presented for both positions of the slit in Fig. 5. LOS velocities profile along $PA=342^{\circ}$ shows that the maximum velocity of rotation of NGC 2535 corresponding to the flat parts of rotation curve is $V_{rot} \sin i \approx 70 \text{ km s}^{-1}$, in a good agreement with Amram et al. (1989) data, who observed this system in H_{α} line.

Unlike NGC 2535, velocity profile along the diameter of its satellite has a peculiar shape: LOS velocity of gas grows with radial distance, but at $R > 5$ arcsec (1.4 kpc) its sign reverses with respect to the centre, so at $R > 10$ arcsec the rotation changes its direction to the opposite one at both sides from the centre. This result slightly differs from Amram et al. (1989) data, which also reveal the rapid decrease of rotation curve, however the velocity does not cross a zero. The kinematical profile of the satellite obtained by Klimanov et al. (2002) agrees in general with our data. Such velocity profile may be explained by strong bending of the gaseous disc, so that at $R \approx 10$ arcsec disc inclination passes through zero. However most probably it reflects non-circular ordered gas motions due to stellar bar, clearly visible in the center of this galaxy. Unlike gas velocities, the stellar LOS velocities remain constant along the radius. To clarify the gas and stellar motions in this region, 2D velocity field is needed.

Velocity profile along the second slit $PA=147^{\circ}$ confirms a very low velocity change along the bridge between the galaxies (at about $20\text{--}30 \text{ km s}^{-1}$). When crossing the spiral arm of NGC 2536, a velocity gradient is observed which may be accounted for galaxy rotation. Stellar velocity profile slightly disagrees with the gaseous one along the slit: it is $20\text{--}40 \text{ km s}^{-1}$ higher than the latter in the bridge and remains less disturbed where the slit crosses the blurred spiral arm of the satellite.

Velocity dispersion of gas is relatively low for both spectral cuts: judging from H_{α} data, which give the most precise estimates, it does not exceed 50 km s^{-1} with the exception of the central region of both galaxies, where small central bars are observed, and probably of the outer low brightness regions of the satellite ($PA=147^{\circ}$). Between the galaxies as well as in the low-contrast spiral arm-bridge velocity dispersion of emission gas has the lowest values (about 30 km s^{-1}), which coincides with the H I velocity dispersion according to Kaufman et al. (1997).

Note that in the main body of NGC 2535 the gas velocity dispersion decreases along the radius parallel with the brightness of emission lines, which suggests that the kinetic energy of random gas motion in the emission regions is connected with the intensity of local star formation there (see also Moiseev et al. 2015, for similar correlation in other galaxies).

Of special interest are the areas of low brightness of

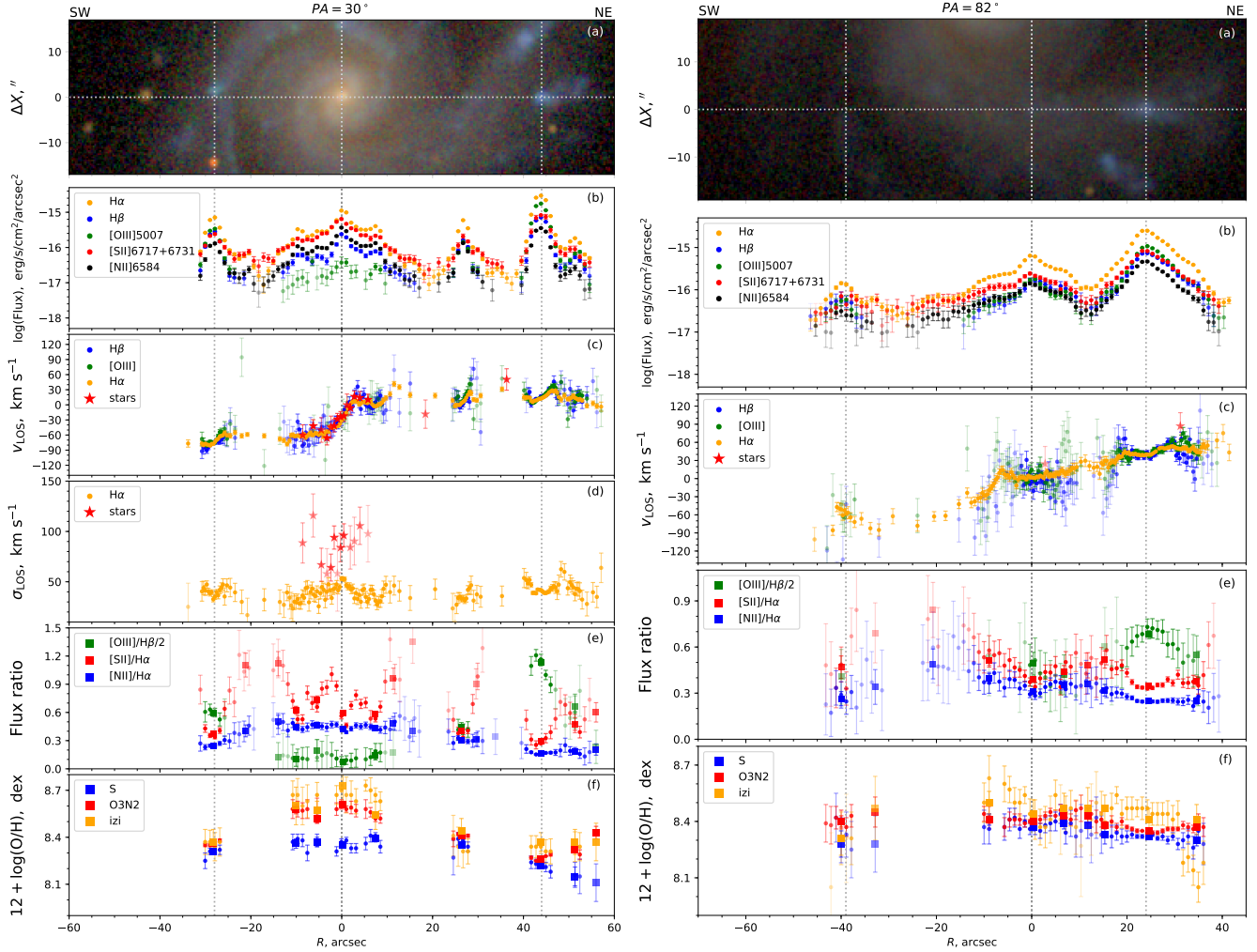


Figure 3. The radial variation of measured parameters for $PA_1 = 30^\circ$ (left panel) and $PA_2 = 82^\circ$ (right panel) for Arp 42. From top to bottom: the slit positions overlaid on the SDSS *gri*-images (a); observed emission lines fluxes (b); LOS velocity (c); LOS velocity dispersion (d); flux ratios (e); and oxygen abundance (f). Circles correspond to the different emission lines. Stars demonstrate the stellar kinematical data. Square symbols show the values obtained after stacking of several adjoining pixels corresponding to single star-forming clumps or to extended regions of fainter emission (see Section 4). For clarity we mark the estimates having large uncertainties relative to other points at a given plot by pale-colored symbols.

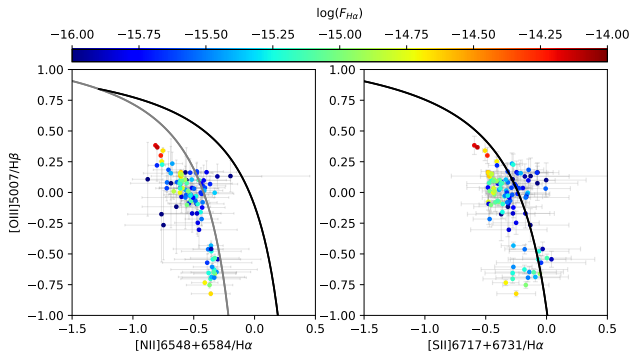


Figure 4. BPT-diagrams plotted for individual bins along the slit for Arp 42. The ‘maximum starburst line’ (Kewley et al. 2001) separating photoionised H II -regions and all other types of gas excitation is shown in black; grey line from Kauffmann et al. (2003) separates the regions with composite mechanism of excitation. Colour denotes the H_α -flux.

emission lines crossed by slits. As it follows from the diagnostic diagrams, (see Fig.6), both faint and bright emission regions, have a photo-ionization as the main mechanism of excitation. However there are few exceptions where the input of collisional excitation, enhancing the $[S\ II]$ vs H_α ratios, may be significant. It is noteworthy that all these cases relate to faint emission regions with low H_α -flux values.

An oxygen abundance of gas was found by several different methods based on the relative intensities of bright emission lines. The results are shown in Fig 5 (bottom left and right panels). The (O/H) distribution along the line connecting the centers of two galaxies (Fig 5, bottom left-hand panel) reveals a significant negative gradient of (O/H) along the slit within the distance ~ 20 arcsec from the nucleus of NGC 2535 especially for the *izi* method. At the same time the profile (O/H) along $PA = 147^\circ$ evidences the nearly constant abundance along the tidal bridge: (O/H) decreases at about 0.2 dex within 80 arcsec, or 22 kpc length. In accordance with expectation, gas metallicity in the bridge between

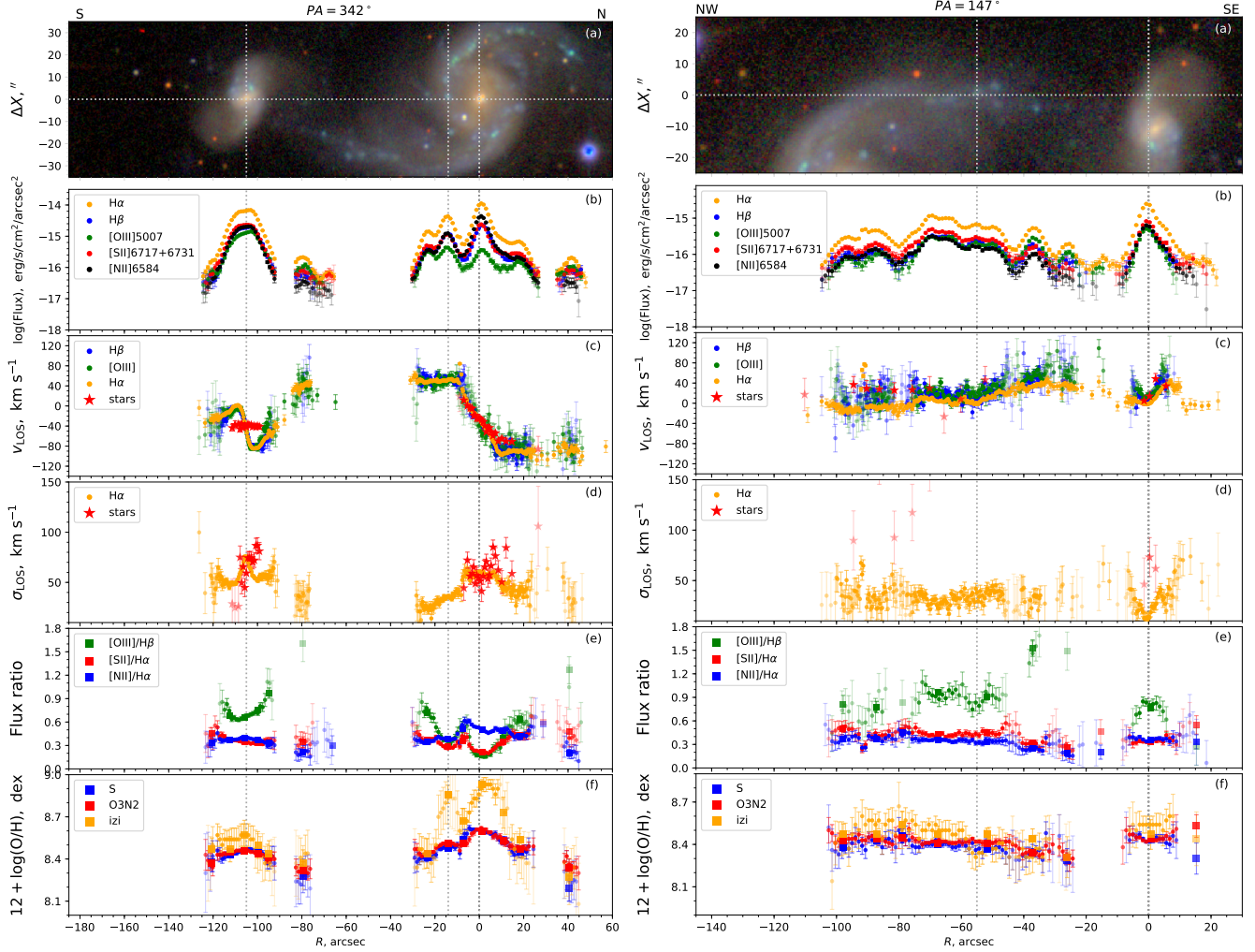


Figure 5. Same as in Fig. 3, but for Arp 82 $PA = 342^\circ$ (left) and $PA = 147^\circ$ (right)

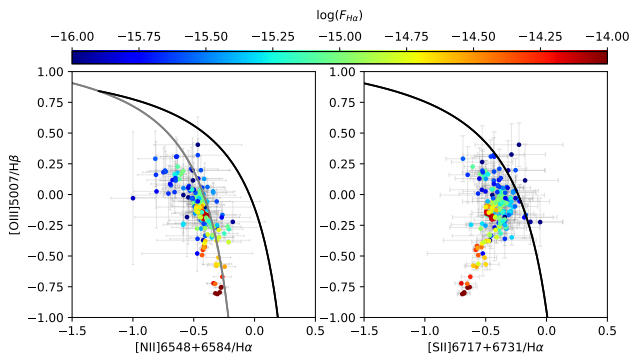


Figure 6. Same as in Fig. 4, but for Arp 82.

galaxies corresponds to metallicity of the outer regions of the main galaxy confirming that it consists of gas expelled from the disc periphery.

5.3 Arp 58

For this system we obtained one spectral cut with the slit passing at a distance 2 arcsec (which is close to the seeing) from the center of the satellite (see Fig. 1, bottom panel). The results of the measurements are illustrated in Fig. 7.

The difference of systemic velocities of two galaxies in the system is about 60 km s^{-1} , and the highest LOS velocity of the main galaxy overlaps with the lowest velocity of its satellite at the side faced to UGC 4457. Nevertheless the profiles of LOS velocities of both galaxies are different. The main galaxy, unlike its companion, demonstrates a regular rotation. The measured velocity gradient of stellar population in the central part of the galaxy is a little lower than for the emission gas, which may be accounted for higher stellar velocity dispersion in the centre. In contrast, a velocity profile of the companion is very asymmetrical. It reveals nearly constant velocity in the NW part of the satellite (towards the main galaxy), which is close to the stellar velocity in the centre of galaxy, and a steep velocity gradient on the opposite side from the centre. It can indicate the outflow of gas or a strong distortion of gaseous layer, which is not unexpected

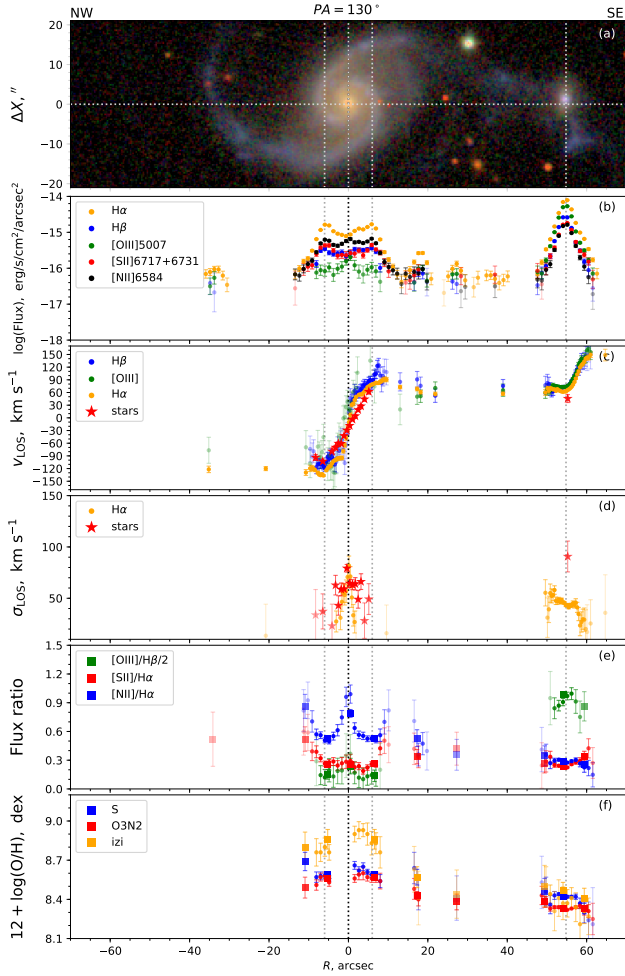


Figure 7. Same as in Fig. 3, but for Arp 58.

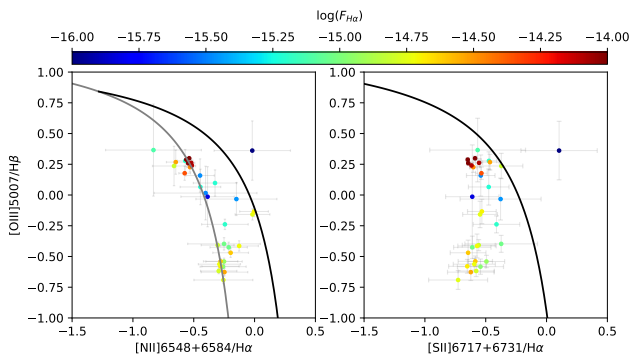


Figure 8. Same as in Fig. 4, but for Arp 58.

if to take into account the very disturbed appearance of this galaxy.

We managed to estimate velocity dispersion of gas and stars for the central parts of galaxies only. As in the other two Arp' systems it does not exceed 50 km s^{-1} for the emission gas. Curiously, stellar velocity dispersion for the main galaxy is lower than for its satellite evidencing the absence of a significant bulge there.

Oxygen abundance distribution along the slit demon-

strates a decreasing of (O/H) with the distance from the centre of UGC 4457, however different methods of abundance estimate we used give different absolute values of (O/H) and its gradient (see the Discussion below).

Fig. 8 compares line ratios for different regions of Arp 58. Their positions at the BPT diagrams correspond to the normal H II regions formed by young stars or to the composite mechanism of excitation. The only outlier point belongs to the center of satellite.

6 DISCUSSION

Below we discuss the main results of photometric and spectral data analysis for three systems in question separately.

6.1 Arp 42

Dynamic mass of the spiral galaxy NGC 5829 (a component of Arp 42) may be estimated only roughly. Assuming the photometrically defined inclination $i \approx 48^\circ$ given by HYPERLEDA, we obtain the velocity of rotation of the outer disc V_{rot} of about $110\text{--}135 \text{ km s}^{-1}$. It is in agreement with HYPERLEDA database, which gives $V_{rot} = 115 \pm 3 \text{ km s}^{-1}$ based on the line width of H I. Total mass within the optical radius may be taken as $M(R_{25}) = k \times V_{rot}^2 R_{25} / G$ where $k=1$ for spherical mass distribution and 0.6 for the flat disc model (Nordsieck 1973). In the former, most expected, case $M(R_{25}) \approx (6 \pm 1) \times 10^{10} M_\odot$. It agrees with the total stellar mass $M_* \approx 5 \times 10^{10} M_\odot$ found from photometry of g and r -band images.

Oxygen abundance in the inner part of the galaxy is $12 + \log(\text{O}/\text{H}) = 8.4\text{--}8.6$ for O3N2 and IZI methods, and $8.3\text{--}8.4$ for S method. It is not in conflict with its stellar mass, at least for O3N2 method (see, e.g., the stellar mass-oxygen abundance relationship for O3N2 method in Sánchez et al. 2017), and also agrees with the high relative mass of gas (H+He): $\mu = \frac{M_{gas}}{M_* + M_{gas}} \approx 0.35$ (see Fig. 10 in Hughes et al. 2013).

Oxygen abundance does not reveal a flattening of radial profile $\log(\text{O}/\text{H})$ at least up to R_{25} (see Fig 3), which is often observed in interacting galaxies (see f.e. Rosa et al. 2014). All methods we used demonstrate a smooth decreasing of O/H along the radius with gradient $0.05\text{--}0.1 \text{ dex at } R_{25}$, see Section 6.4. The directly observable gradient is lower along the slit $\text{PA} = 82^\circ$ because this slit does not pass through the galactic centre.

As it was noted in the Introduction, the most spectacular features of gas-rich spiral galaxy NGC 5829 are two extended emission regions containing two bright clumps BER1,2, in the bifurcated northern spiral arm (see Fig. 1).

We estimated colour indices of compact stellar regions BER1,2 from the photometry of SDSS images and corrected them for Galactic extinction and internal extinction calculated from the H_α/H_β ratio: $E_{B-V} \approx 0.4$. Their g -magnitudes taken with the surrounding bright emission area of several kpc-size, are 17.1^m and 17.6^m (not corrected for the extinction), while g -magnitudes of the compact clumps BER1, BER2 within the 4 arcsec aperture are 18.2^m and 17.8^m respectively, which corresponds to luminosities $(4\text{--}6) \times 10^8 L_\odot$.

Taking into account their blue $g-r$ colours 0.12, 0.16 respectively (corrected for Galactic extinction according to [Schlafly & Finkbeiner \(2011\)](#)), their stellar masses in the model ([Bell et al. 2003](#)) are $(2-3) \times 10^8 M_\odot$. It exceeds typical masses of globular clusters, being closer to a mass of a dwarf galaxy (for the usually accepted IMF). Accounting for total extinction in g,r -bands has little effect on the determination of the stellar mass, since it increases the estimate of the luminosity and about the same decreases the mass to luminosity ratio.

At any rate, BER1,2 are much more luminous than so-called stellar super-clusters observed in many strongly interacting or merging galaxies rich of gas, such as Antennae where they have properties expected for young massive globular clusters ([Whitmore et al. 2010](#)). The most luminous of the Antennae' superclusters have absolute magnitude $M_V = -(13 - 14.6)$, corresponding to luminosity $(1-6) \times 10^7 L_\odot$ - that is they are much fainter than BERs! To avoid the conclusion about the enormously big mass of these stellar clumps one can admit a bottom-light IMF of their stellar population.

Note however, that the Antennae system is at a distance of 22 Mpc (against a distance of 78 Mpc for Arp 42), and the mentioned observations ([Whitmore et al. 2010](#)) were carried out with very high quality (HST). SDSS resolution does not allow to resolve the images of bright clumps, but they look definitely not as point-like sources. The aperture 4 arcsec which was applied to the clumps corresponds to the diameter about 1.5 kpc. Evidently, both BER1,2 are the combination of several bright young stellar complexes (superclusters), surrounded by the extended zone of several kpc size of emission gas and active star formation.

Extinction-corrected positions of BER1,2 are represented as open stars in the two-colour diagram shown in Fig. 9. They are in satisfactory agreement with Starburst99 ([Leitherer et al. 1999](#)) model tracks for both continuous and instantaneous star formation (for Kroupa IMF [Kroupa 2001](#)) and confirm their very young stellar age: $t = 5 - 14$ Myr. In turn, the central part of the galaxy (open hexagon), better fits with the model for continuous star formation and evidently consists of a mixture of stars of different ages, so its luminosity-weighted age of stellar population is about 4 billions yr. For the comparison we also overplot the position of three most luminous clumps of star formation in the opposite spiral arm of NGC 5829 (filled stars), their position is shown by circles in Fig. 1. As one can see, all considered stellar clumps are the regions of current or very recent star formation. At the same time, BER1,2 overwhelm other young stellar complexes by luminosity and probably by stellar mass significantly.

What caused a simultaneous burst of star formation in two small regions observed at close branches of a bifurcated spiral arm, remains a puzzle. It is possible that they are not unique, we just catch two star-forming regions in the most luminous phase. These compact regions could not be the fragments of a dwarf galaxy crossing a disc of the parent galaxy, inspiring a strong shock wave and gas compression, because BERs seem to be connected with spiral arms, and they do not reveal a significant velocity shift with respect to the adjacent regions. It is worth noting that in the northern half of the galaxy where BERs are observed, a spiral pattern is significantly smoothed or destroyed. As far as we don't see any companion which evidently may be responsible for the

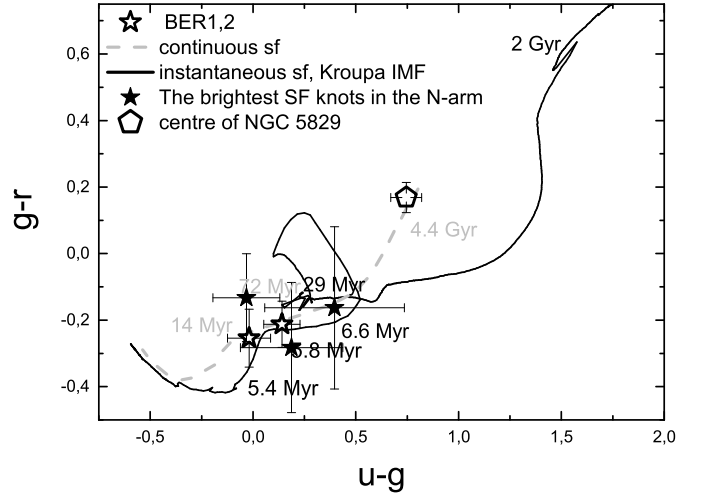


Figure 9. The $(g-r)$ vs $(u-g)$ diagram for NGC 5829. Open stars show the positions of BER1 and BER2. Filled stars and hexagon relate to the bright local sites of star formation in the opposite spiral arm and to the central part of NGC 5829. Black line and gray dashed line follow Starburst99 model tracks for instantaneous and continuous star formation respectively. We mark the ages of stellar population corresponding to the closest regions of the tracks by black and gray printing type for instantaneous and continuous star formation models correspondingly.

distortion of structure of NGC 5829, the possibility remains that the latter is a result of recent accretion of gas falling onto a northern part of a disc from outside. The accreting gas could strongly enhance star formation in the regions where the flow meets the dense native gas concentrations in spiral arms. However, the oxygen abundance radial profile does not show any signs of dropping in the region of BERs, which in the case of accretion could indicate that either a falling gas is pre-enriched, or the mass of absorbed gas is too small to affect chemistry. More detailed data on the neutral gas dynamics and distribution are needed to verify it.

The spectra of BER1,2 stand out for their high $[O\text{ III}]/H\beta$ ratios while having rather moderate $[S\text{ II}]/H\alpha$ and $[N\text{ II}]/H\alpha$ ratios. It seems that the $H\text{ II}$ regions around both stellar superclusters containing massive stars are density bound, so that a significant fraction of ionizing photons is leaking in the surrounding gas.

Curiously, all three emission regions crossed by the slit $PA=30^\circ$, including BER1, reveal velocity gradients within the range 5–7 arcsec (2–3 kpc), which may be interpreted as the rotation with respect to the surrounding disc at the same direction as the disc as whole. It is compatible with the idea that these regions were formed by the compression of rotating gas in the disc. Still it is not evident that the gas is gravitationally bound at this scale. Note however that if to admit that these regions are close to be virialized, their masses should be an order of a few $10^8 M_\odot$, which is compatible with the mass estimate of stellar population in BER1.

The second spectral cut at $PA=82^\circ$ does not demonstrate any significant velocity gradient across the similar-looking emission region BER2. If both young massive stellar complexes – BER1 and 2 – have a similar age and the formation

mechanism, which seems natural, then their observed kinematic differences evidence that they do not present a gravitationally coupled systems at kpc-scale. Of course, there remains a possibility that they are strongly flattened and dynamically isolated configurations observed at different inclination angles (nearly face-on in the case of BER2).

It is not surprising that the massive stellar complex distorts the velocity field around it. Indeed, our observations demonstrate the enhanced non-circular gas motions within the region of several kpc-size around BER1, however similar behavior of LOS velocities also takes place in another bright emission region crossed by slit PA 30° closer to the centre, in spite of the absence of compact stellar source there.

The second star-forming clump, BER2, does not demonstrate any velocity peculiarity. So far as there is no ground to consider BERs as dynamically detached regions. They belong to a disc population and formed recently in the spiral arm branches as the result of some strongly non-stable process.

6.2 Arp 82

Total luminosity L_r of NGC 2535 is $1.6 \times 10^{10} L_\odot$, and the stellar mass M_* corresponding to its colour ($g-r$), obtained from SDSS image, is $5.6 \times 10^{10} M_\odot$ for Bell et al. (2003) model of stellar population. Similarly found stellar mass for NGC 2536 is $8.7 \times 10^9 M_\odot$. Based on the mass-metallicity relation described in Sánchez et al. 2017 for the O3N2 calibrator, these mass values agree with the oxygen abundances of galaxies (8.5 - 8.6 for NGC 2535 and about 8.4 for NGC 2536).

Our observations confirm the regular rotation of NGC 2535 and a smooth velocity distribution along the bridge, connecting two galaxies. In contrast, there is a strong non-circular gas motion in the satellite galaxy – both in the central part and in the spiral arm adjacent to the bridge. At the same time the velocity dispersion of emission gas, estimated from the linewidths, remains low along the bridge, evidencing the laminar flow of gas, being a little shifted by velocity from the stellar component of the bridge.

To find out the age of stellar population in the starforming sites of Arp 82, in Fig. 10 we show the position of selected emission regions crossed by the slits between the main body of NGC2535 and its satellite, as well as for the central part of NGC2536 (identified with circles in Fig. 1) at the ($g-r$) vs ($u-g$) diagram. Colours were estimated from the photometry of SDSS images and corrected for extinction calculated from the H_α/H_β ratio: $E_{B-V} \approx 0.15$. The local sites of star formation in the spiral arm (bridge) are shown by stars, the hexagone gives the position of the satellite. Open star corresponds to the diffuse region between galaxies where the bridge spiral arm seems to be splitting (see below).

Evolution tracks in the Fig. 10 are shown for two models: instantaneous star formation (black line) and constant star formation rate (gray dashed line). Colours of the regions encircling blue stellar clumps and diffuse emission in the spiral arm (bridge) marked by stars are in good agreement with the model track for instantaneous star formation and correspond to the prevailing input of the light of young stars, so their luminosity-weighted age is less than 10 Myr (most probably, in the range 7.5-8 Myr).

The situation is different for the other emission regions. One of them, denoted by open star, is situated in the low

brightness bifurcated part of spiral arm NGC2535. The other two regions lie in the bridge: one is the closest to NGC2535 and the second relates to the diffuse emission region close to NGC 2536. These three areas are better described by the model with continuous star formation and definitely contain not only young, but also the older stars: their colours agree with constant star formation rate during the last several billion yr (2-6 Gyr). The same is correct for the central region of NGC 2536 which definitely has a large age.

As it follows from the abundance profile for PA=147° there is a jump of (O/H) at about 0.2 dex between the bridge and the off-center regions of the main body of a small galaxy NGC 2536 (the abundance of gas in the satellite is higher than in the adjoining regions closer to the main galaxy). It allows to propose that the gaseous bridge does not mix with the gas observed in the satellite. The same conclusion follows from the spectral cut at PA=342°: the oxygen abundance in the satellite is higher than in the neighbour extended emission "island" located closer to the main galaxy. This region belongs to the bridge rather than to the satellite, because its LOS velocity lays at the continuation of the velocity profile of NGC 2535, and differs at about 80 km s⁻¹ from the central velocity of the satellite. The oxygen abundance of this region coincides with that observed in the bridge (see Fig. 5).

The absence of clear signs of gas exchange between galaxies agrees with Klaric' dynamic model of the interacting system, which shows that the bridge intersects NGC 2536 only in projection, so the satellite is a little closer to us (see Kaufman et al. 1997). In this case the enhanced star formation in the satellite is not a result of collision with the gas flowing along the bridge, but rather is caused by internal processes triggered by tidal disc disturbance.

The other interesting feature of NGC 2535 is the faint trace of the third spiral arm, which branches off the bright arm running to the satellite. First it was noted by Hancock et al. (2007). A faint branch is easily visible at the SDSS and GALEX images in Fig. 11, where the direction of branching spiral arms are marked by arrows. This narrow arm possesses blue color and looks symmetric with respect to opposite, northern arm. It seems that we see the residual arm of symmetric (in the past) spiral structure of the galaxy, existed before the encounter happened. Most probably, a tidal force imposed a new mode of the density wave in the disc, which gave rise to the arm-bridge, while the previous mode had not yet time to die totally out. Note in advance that similar feature is also noticeable in Arp 58 (see the next subsection).

6.3 Arp 58

In many respects this system is similar to Arp 82, described in the previous section, although it is less studied, and the masses ratio of the main galaxy and the satellite in Arp 58 is significantly higher than in the former case. In both systems we have a long tidal tail of the main galaxy and a bluish bridge-like spiral arm, connecting two galaxies. Most probably, this arm does not end on the satellite galaxy, but rather pass a little further projecting onto it. For Arp 82 a similar proposal was argued above, and in the case of Arp 58 such possibility is based on the colour image of the system, especially in UV light (see the combined FUV and NUV GALEX image in Fig. 12), where the blue spiral arm looks projecting

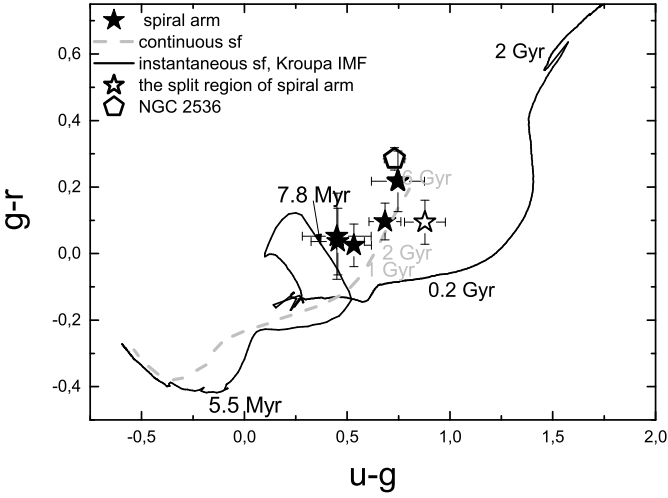


Figure 10. The $(g-r)$ vs $(u-g)$ diagram. Filled stars show the position of star forming sites in the spiral arm of NGC 2535. Open star relates to the diffuse region of the spiral bridge. Open hexagon gives the position of the small companion galaxy NGC 2536. Black and gray lines demonstrate Starburst99 model tracks for instantaneous and continuous star formation respectively. We mark the ages of stellar population corresponding to the closest regions of the track by black and gray printing type for instantaneous and continuous star formation models correspondingly.

on the satellite galaxy. In this case a blue ejection-like feature emanating from the body of a satellite may be considered as the continuation of UV bridge-arm of the main galaxy. A noticeable dark gap between this feature and the satellite is especially prominent in the UV GALEX image, which, if it is accounted for the dust extinction in the satellite, evidences that the bridge arm is behind the satellite.

Another curious detail that is evident from the UV-image is the faint offshoot of the spiral arm-bridge at about a half-way between the centers of the galaxies. This thin arc-like spur looks symmetric with respect to the opposite arm of the main galaxy, similarly to that in Arp 82.

A symmetric gas velocity profile of UGC 4457 allows to restore its rotation velocity curve. It is presented in Fig 13 for the adopted inclination angle $i = 65^\circ$ and position angle $(PA)_0 = 164.4^\circ$ taken from HYPERLEDA. The curve grows slowly, reaching maximum or flat region of the curve at about 11–12 arcsec, although the presence of non-circular gas motion is evident at larger distances. The ‘knee’ (a change of gradient of gaseous velocity curve) at $R \sim 3\text{--}6$ arcsec most probably does not reflect a mass distribution: at these distances the slit crosses the bright spiral arm where radial non-circular velocities are quite expected.

The main galaxy in Arp 58 does not possess a noticeable bulge, so the upper limit of mass of stellar population of the disc may be estimated if to admit that its circular velocity does not exceed the maximal measured velocity of rotation, reaching $V_{\max} \sim 230 \text{ km s}^{-1}$ at $R=R_{\max} \approx 12$ arcsec. For a disc with exponential mass distribution it corresponds to the dynamic mass $M_{\text{disc}} < 1.2 V_{\max}^2 R_{\max} / G = 1.26 \times 10^{11} M_\odot$. Accounting for dark halo may reduce this value. This limit agrees with the mass of stellar population based on the photometry of SDSS



Figure 11. Combined GALEX FUV and NUV-bands with overplotted arrows showing the position of bifurcated spiral arms (top) and SDSS images of Arp 82 (bottom).

image which gives a slightly lower mass value. Indeed, we found the total luminosity of galaxy $L_r \approx 3.2 \times 10^{10} L_\odot$ and the observed $g-r = 0.68$ (corrected for Galactic extinction), corresponding to $M_*/L_r \sim 2.8$ solar units according to the model of Bell et al. (2003), which gives $M_* \approx 9 \times 10^{10} M_\odot$. Here the internal extinction is ignored; taking it into account will reduce the mass estimate due to the lower colour index and M_*/L_r ratio, however it will be compensated by the decreasing of L_r . Note that the estimation of dynamical mass is also very preliminary. The additional velocity measurements are needed to clarify $(PA)_0$ of major axis and the inclination angle of the disc.

The emission regions between two galaxies, crossed by the slit, keep their LOS velocity close to those observed in the adjacent part of UGC 4457. Unlike UGC 4457, the satellite does not reveal a regular rotation: its half faced to the main galaxy demonstrate a zero LOS velocity gradient which is evidently the result of gravitational interaction. It does not allow to get the dynamic mass. Photometric method which uses SDSS images (g and r -bands) gives for a small galaxy

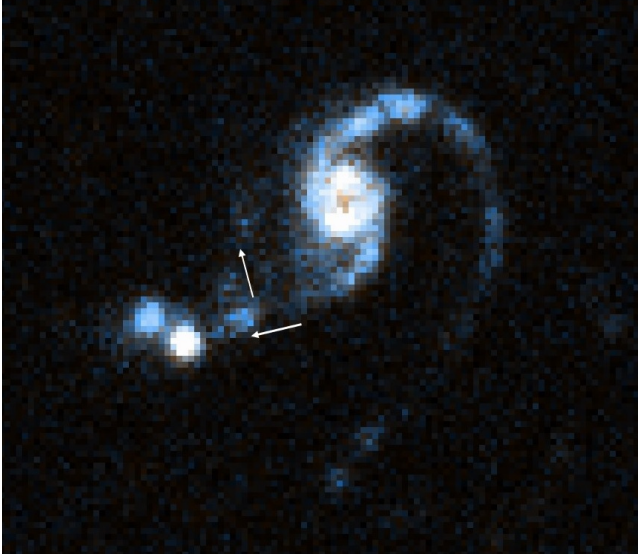


Figure 12. Combined GALEX FUV and NUV-bands image of Arp 58 with overlaid arrows showing the position of bifurcated spiral arms.

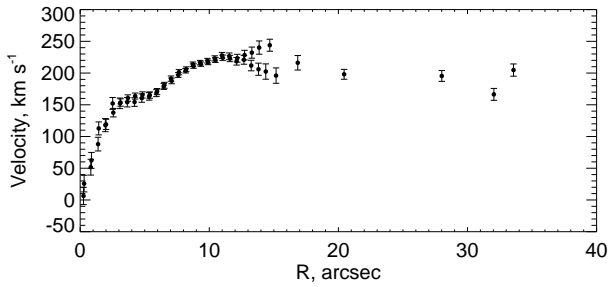


Figure 13. The H_α rotation curve of Arp 58.

$M_* \approx 8.5 \times 10^8 M_\odot$ and $M/L_r = 0.71$ solar units (not corrected for inner absorption).

Line intensity ratios at the BPT diagrams show that the emission regions in Arp 58 correspond to H II-spectra of photoionized gas and – in some regions – to the composite spectra. A special case is the single outlier at the diagrams in Fig. 8 for Arp 58, revealing the highest ratios of ion-to- $H\alpha$ lines intensities. It belongs to the extended emission region in the center of the satellite galaxy, and may be considered as the indirect evidence of the moderate AGN-activity.

6.4 Oxygen abundance gradients

Fig. 14 shows the profiles of oxygen abundance as a function of the inclination-corrected distance from the centre of the main galaxy (reduced to its disc plane for the adopted inclination angle) and their linear fits for all three galaxies. This figure excludes all points with the suspected significant contribution of non-photoionization mechanism of excitation according to their positions at the diagnostic diagrams. Here we remind the reader that all regions with the suspected DIG contribution having $EW(H\alpha) < 3$ have also been excluded from the analysis. In order to rely on the high S/N data we use the estimates obtained for stacked spectra only (squares in Figs. 3, 7, 5) for estimating the metallicity gradients.

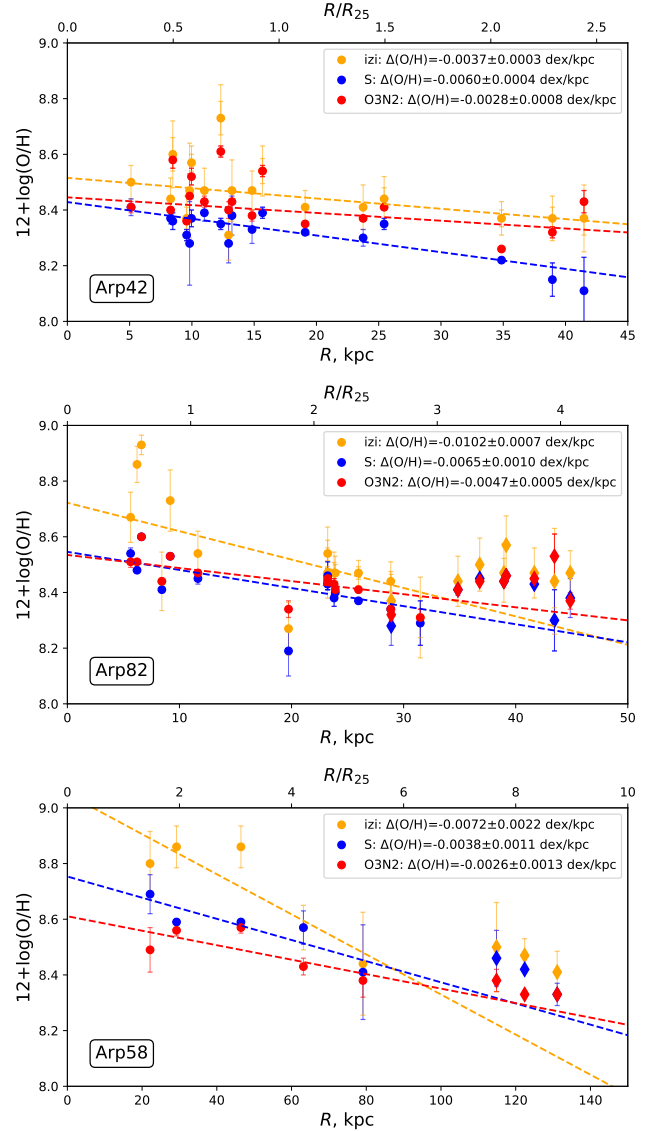


Figure 14. From top to bottom: the radial profiles of oxygen abundance of Arp 42, Arp 82 and Arp 58 (reduced to the disc plane of the main galaxy). The gradients were estimated by robust least-square fitting of the values for a disc of the main galaxy. The points related to the satellites are denoted by diamonds (assuming that they lay in the disc plane).

In all three cases the gradients are shallow, not exceeding $-0.01 \text{ dex kpc}^{-1}$. It agrees with the lower abundance gradients usually found for galaxies in close pairs (Kewley et al. 2010; Rosa et al. 2014) and for interacting or merging galaxies (Rupke et al. 2010; Rich et al. 2012) in comparison with single galaxies, which may be accounted for the radial mixing of gas inspired by interaction. It is interesting, that at large radial distances the flattening of gradient is often observed even for non-interacting galaxies (Sánchez et al. 2014; Sánchez-Menguiano et al. 2016, 2018), that is the mean abundance gradient decreases when the outskirts of galaxies are taken into consideration. Two of the studied systems reveal similar behaviour. The abundance gradients we estimated were measured along the radial coordinate (corrected for the disc inclination), including the regions of tidal bridges in Arp 82 and Arp 58. Taken separately, these outer regions do not re-

veal a clear evidence of any gradient of O/H, which explains the flattening of the abundance profiles. However, we need more observations at this radial range to confirm it.

It is known that a spread of (O/H) gradients in galaxies are lower when normalized to the physical radial scale such as the isophote radius R_{25} or effective radius R_e (Sánchez et al. 2014; Sánchez-Menguiano et al. 2016, 2018). Indeed, the mean gradients for three systems we consider become very similar if to express them in terms of R_{25} : they lay between -0.05 and -0.1 dex R_{25}^{-1} , which is significantly lower than for normal spiral galaxies ($-0.3 - 0.4$ dex R_{25}^{-1} according to Pilyugin et al. 2014; Ho et al. 2015).

7 GENERAL CONCLUSIONS

Our long-slit observations confirm that the systems we studied are dynamically disturbed and actively star-forming galaxies. They contain many emission knots (clumps) together with the extended emission regions of low brightness. The mean ages of stellar clumps found from *ugr*-photometry are very low and (with a few exceptions) exclude a notable contribution of old stellar population in their luminosity. A special interest present two extremely luminous compact clumps (BER-1,2) in the bifurcated spiral arm in Arp 42, which origin remains a puzzle. Their luminous masses within the scale of 1-2 kpc should exceed $10^8 M_\odot$ unless their stellar IMF is not "bottom-light". The interaction with some 'dark' dwarf galaxy or the gas accretion triggering the formation of super stellar clusters may not be excluded.

LOS velocity profiles in the viewed galaxies reveal local regions of non-circular gas motions, which usually coincide with bright star-forming sites. M51-type systems Arp 82 and Arp 58 demonstrate a regular rotation of the main galaxies, a low velocity gradient along bridges and a strong non-circular motion of gas in their satellites evidently caused by interaction. In both systems there observed faint arc-like offshoot from the bridge spiral arms, looking symmetrical with respect to the opposite bright arms of the main galaxy. It allows to propose that in these galaxies we observe a transient two-mode wave spiral structure: while a spiral arm looking as a bridge between galaxies was induced by tidal interaction, the original spiral arm which existed before the close encounter, faded, so that we can observe only its weak trace.

At the diagnostic diagrams the low brightness areas are situated on both sides of the demarcation line, separating the area of stellar photoionization from shock excitation or hard radiation area. However in all systems we consider the low brightness emission regions prevail among those demonstrating the composite spectra, especially standing out for their enhanced $[N II]/H\alpha$ ratios. It reveals the presence of low brightness diffuse ionized gas in the systems, for which a harder ionization is needed to account for the line ratios. (Note that these regions were not used for the abundance estimations).

Among the commonly invoked sources of additional ionization are the radiation of old hot pAGB stars, the leakage of hard photons from the star-forming regions, and the shock waves (see discussion in Zhang et al. 2017). The first mechanism is less likely because of very low brightness of old stellar population in the considered regions. The leakage of hard photons from the unresolved H II regions looks quite

acceptable. The most outstanding case of LINER-like spectrum is the nucleus of the satellite galaxy in Arp 58, where the line ratios give evidence of the low level of AGN activity in this small galaxy, inspired by gravitational perturbation.

The presence of shock waves is natural to expect in the interacting systems. Indeed, shock waves caused by interaction of tidally expelled gas with the ambient circumgalactic gas, or by collisions of disturbed gas flows in tidal debris, may trigger star formation beyond the main bodies of galaxies even in the regions of initially low gas density. It agrees with numerical simulations, which confirm that the strong compression and shocks produced by the galaxy interaction fuel rapid formation of stellar clusters after the first close pericentric passage (see e.g. Maji et al. 2017).

The limited spectral and spatial resolution of our observations did not allow to reveal shock waves directly. A non-direct evidence of their presence may be the enhanced velocity of gas turbulent motions in the regions, where the velocity dispersion exceeds the value $20-40 \text{ km s}^{-1}$, usually observed in H II regions of galaxies. The existing model estimates show that the enhanced velocity dispersion of emission gas may account for the line ratios of the composite LINER-like spectra at the diagnostic diagrams (see e.g. Rich et al. 2011) in agreement with observations of galaxies (Oparin & Moiseev 2018).

However in the case of our systems the regions where the velocity dispersion reaches or exceeds 50 km s^{-1} are rare. Most evidently, they include the central regions of both galaxies and the bright area in the base of spiral bridge between galaxies in the system Arp 82. As expected, their positions at BPT diagram reveal a composite spectra.

All considered galaxies have low gradient of (O/H) along the radius of central galaxy which does not exceed $-(0.003 - 0.005) \text{ dex kpc}^{-1}$ for Arp 42 and Arp 58 and $-(0.005 - 0.01) \text{ dex kpc}^{-1}$ for Arp 82 if not to count its satellite (see Fig. 14). If to express the gradients in terms of R_{25} : they lay between -0.05 and -0.1 dex R_{25}^{-1} , which is significantly lower than for normal spiral galaxies ($-0.3 - 0.4$ dex R_{25}^{-1} according to Pilyugin et al. 2014; Ho et al. 2015). It allows to conclude that the gas in their discs was partially expelled outwards as the result of interaction (at least for the last two galaxies). However the oxygen abundance of the central regions of galaxies we consider in general agrees with the "metallicity-stellar mass" dependence for non-interacting galaxies. There is no clear evidence of gas collision or gas chemical mixing between the main galaxies and their satellites in M 51-type systems Arp 82 and Arp 58.

ACKNOWLEDGEMENTS

The authors are grateful to anonymous referee for valuable comments that helped to improve the manuscript. They also thank V.Afanasyev and R.Uklein for a collaboration. The observations at the 6-meter BTA telescope were carried out with the financial support of the Ministry of Education and Science of the Russian Federation (agreement No. 14.619.21.0004, project ID RFMEFI61914X0004). The reduction of the spectral data were supported by The Russian Science Foundation (RSCF) grant No. 17-72-20119. The estimate of the metallicity and its interpretation were supported by Russian Foundation for Basic Research grant

No. 18-32-20120. The authors acknowledge the usage of the HyperLeda database (<http://leda.univ-lyon1.fr>). Authors acknowledge support from the Leading Scientific School in astrophysics (direction: extragalactic astronomy) at Moscow State University. Funding for the Sloan Digital Sky Survey IV has been provided by the Alfred P. Sloan Foundation, the U.S. Department of Energy Office of Science, and the Participating Institutions. SDSS-IV acknowledges support and resources from the Center for High-Performance Computing at the University of Utah. The SDSS web site is www.sdss.org.

SDSS-IV is managed by the Astrophysical Research Consortium for the Participating Institutions of the SDSS Collaboration including the Brazilian Participation Group, the Carnegie Institution for Science, Carnegie Mellon University, the Chilean Participation Group, the French Participation Group, Harvard-Smithsonian Center for Astrophysics, Instituto de Astrofísica de Canarias, The Johns Hopkins University, Kavli Institute for the Physics and Mathematics of the Universe (IPMU) / University of Tokyo, Lawrence Berkeley National Laboratory, Leibniz Institut für Astrophysik Potsdam (AIP), Max-Planck-Institut für Astronomie (MPIA Heidelberg), Max-Planck-Institut für Astrophysik (MPA Garching), Max-Planck-Institut für Extraterrestrische Physik (MPE), National Astronomical Observatories of China, New Mexico State University, New York University, University of Notre Dame, Observatório Nacional / MCTI, The Ohio State University, Pennsylvania State University, Shanghai Astronomical Observatory, United Kingdom Participation Group, Universidad Nacional Autónoma de México, University of Arizona, University of Colorado Boulder, University of Oxford, University of Portsmouth, University of Utah, University of Virginia, University of Washington, University of Wisconsin, Vanderbilt University, and Yale University.

REFERENCES

- Afanasiev V. L., Moiseev A. V., 2011, *Baltic Astronomy*, **20**, 363
- Amram P., Marcelin M., Boulesteix J., Le Coarer E., 1989, *A&AS*, **81**, 59
- Baldwin J. A., Phillips M. M., Terlevich R., 1981, *PASP*, **93**, 5
- Bell E. F., McIntosh D. H., Katz N., Weinberg M. D., 2003, *ApJS*, **149**, 289
- Blanc G. A., Kewley L., Vogt F. P. A., Dopita M. A., 2015, *ApJ*, **798**, 99
- Boquien M., et al., 2009, *AJ*, **137**, 4561
- Bournaud F., 2011, in Charbonnel C., Montmerle T., eds, *EAS Publications Series Vol. 51*, EAS Publications Series. pp 107–131 ([arXiv:1106.1793](https://arxiv.org/abs/1106.1793)), doi:10.1051/eas/1151008
- Butenko M. A., Khoperskov A. V., 2017, *Astrophysical Bulletin*, **72**, 232
- Casasola V., Bettoni D., Galletta G., 2004, *A&A*, **422**, 941
- Chernin A. D., Kravtsova A. S., Zasov A. V., Arkhipova V. P., 2001, *Astronomy Reports*, **45**, 841
- Chilingarian I., Prugniel P., Sil'chenko O., Koleva M., 2007a, in Vazdekis A., Peletier R., eds, *IAU Symposium Vol. 241*, IAU Symposium. pp 175–176 ([arXiv:0709.3047](https://arxiv.org/abs/0709.3047)), doi:10.1017/S1743921307007752
- Chilingarian I. V., Prugniel P., Sil'chenko O. K., Afanasiev V. L., 2007b, *MNRAS*, **376**, 1033
- Duc P.-A., Renaud F., 2013, in Souchay J., Mathis S., Tokieda T., eds, *Lecture Notes in Physics*, Berlin Springer Verlag Vol. 861, *Lecture Notes in Physics*, Berlin Springer Verlag. p. 327 ([arXiv:1112.1922](https://arxiv.org/abs/1112.1922)), doi:10.1007/978-3-642-32961-6_9
- Duc P.-A., Brinks E., Springel V., Pichardo B., Weilbacher P., Mirabel I. F., 2000, *AJ*, **120**, 1238
- Elmegreen B. G., Kaufman M., Thomasson M., 1993, *ApJ*, **412**, 90
- Hancock M., Smith B. J., Struck C., Giroux M. L., Appleton P. N., Charmandaris V., Reach W. T., 2007, *AJ*, **133**, 676
- Hernquist L., 1989, *Nature*, **340**, 687
- Ho I.-T., Kudritzki R.-P., Kewley L. J., Zahid H. J., Dopita M. A., Bresolin F., Rupke D. S. N., 2015, *MNRAS*, **448**, 2030
- Holincheck A. J., et al., 2016, *MNRAS*, **459**, 720
- Howard S., Keel W. C., Byrd G., Burkey J., 1993, *ApJ*, **417**, 502
- Hughes T. M., Cortese L., Boselli A., Gavazzi G., Davies J. I., 2013, *A&A*, **550**, A115
- Kapferer W., Kronberger T., Ferrari C., Riser T., Schindler S., 2008, *MNRAS*, **389**, 1405
- Kauffmann G., et al., 2003, *MNRAS*, **346**, 1055
- Kaufman M., Brinks E., Elmegreen D. M., Thomasson M., Elmegreen B. G., Struck C., Klaric M., 1997, *AJ*, **114**, 2323
- Kewley L. J., Ellison S. L., 2008, *ApJ*, **681**, 1183
- Kewley L. J., Dopita M. A., Sutherland R. S., Heisler C. A., Trevena J., 2001, *ApJ*, **556**, 121
- Kewley L. J., Geller M. J., Barton E. J., 2006, *AJ*, **131**, 2004
- Kewley L. J., Rupke D., Zahid H. J., Geller M. J., Barton E. J., 2010, *ApJ*, **721**, L48
- Klimanov S. A., Reshetnikov V. P., Burenkov A. N., 2002, *Astronomy Letters*, **28**, 579
- Kroupa P., 2001, *MNRAS*, **322**, 231
- Kumari N., Maiolino R., Belfiore F., Curti M., 2019, *MNRAS*, **485**, 367
- Lacerda E. A. D., et al., 2018, *MNRAS*, **474**, 3727
- Le Borgne D., Rocca-Volmerange B., Prugniel P., Lançon A., Fioc M., Soubiran C., 2004, *A&A*, **425**, 881
- Leitherer C., et al., 1999, *ApJS*, **123**, 3
- Levesque E. M., Kewley L. J., Larson K. L., 2010, *AJ*, **139**, 712
- Maji M., Zhu Q., Li Y., Charlton J., Hernquist L., Knebe A., 2017, *ApJ*, **844**, 108
- Makarov D., Prugniel P., Terekhova N., Courtois H., Vauglin I., 2014, *A&A*, **570**, A13
- Marino R. A., et al., 2013, *A&A*, **559**, A114
- Moiseev A. V., Tikhonov A. V., Klypin A., 2015, *MNRAS*, **449**, 3568
- Nishiura S., Shimada M., Ohya Y., Murayama T., Taniguchi Y., 2000, *AJ*, **120**, 1691
- Noguchi M., 1988, *A&A*, **201**, 37
- Nordsieck K. H., 1973, *ApJ*, **184**, 719
- Oparin D. V., Moiseev A. V., 2018, preprint, p. [arXiv:1808.08525](https://arxiv.org/abs/1808.08525) ([arXiv:1808.08525](https://arxiv.org/abs/1808.08525))
- Pilyugin L. S., Grebel E. K., 2016, *MNRAS*, **457**, 3678
- Pilyugin L. S., Grebel E. K., Kniazev A. Y., 2014, *AJ*, **147**, 131
- Renaud F., Bournaud F., Kraljic K., Duc P.-A., 2014, *MNRAS*, **442**, L33
- Reshetnikov V. P., Hagen-Thorn V. A., Yakovleva V. A., 1993, *A&AS*, **99**, 257
- Rich J. A., Kewley L. J., Dopita M. A., 2011, *ApJ*, **734**, 87
- Rich J. A., Torrey P., Kewley L. J., Dopita M. A., Rupke D. S. N., 2012, *ApJ*, **753**, 5
- Rosa D. A., Dors O. L., Krabbe A. C., Hägele G. F., Cardaci M. V., Pastoriza M. G., Rodrigues I., Winge C., 2014, *MNRAS*, **444**, 2005
- Rupke D. S. N., Kewley L. J., Chien L.-H., 2010, *ApJ*, **723**, 1255
- Sánchez-Menguiano L., et al., 2016, *A&A*, **587**, A70
- Sánchez-Menguiano L., et al., 2018, *A&A*, **609**, A119
- Sánchez S. F., et al., 2014, *A&A*, **563**, A49
- Sánchez S. F., et al., 2017, *MNRAS*, **469**, 2121
- Schlafly E. F., Finkbeiner D. P., 2011, *ApJ*, **737**, 103
- Smith R., Duc P. A., Candlish G. N., Fellhauer M., Sheen Y.-K., Gibson B. K., 2013, *MNRAS*, **436**, 839
- Tonnesen S., Bryan G. L., 2012, *MNRAS*, **422**, 1609
- Veilleux S., Osterbrock D. E., 1987, *ApJS*, **63**, 295
- Weilbacher P. M., Fritze-v. Alvensleben U., Duc P.-A., 2002, in Geisler D. P., Grebel E. K., Minniti D., eds, *IAU Symposium Vol. 207*, *Extragalactic Star Clusters*. p. 648 ([arXiv:astro-ph/0107194](https://arxiv.org/abs/astro-ph/0107194))
- Wetzstein M., Naab T., Burkert A., 2007, *MNRAS*, **375**, 805
- Whitmore B. C., et al., 2010, *AJ*, **140**, 75
- Zasov A., Saburova A., Katkov I., Egorov O., Afanasiev V., 2015, *MNRAS*, **449**, 1605
- Zasov A. V., Saburova A. S., Egorov O. V., Afanasiev V. L., 2016, *MNRAS*, **462**, 3419

- Zasov A. V., Saburova A. S., Egorov O. V., Uklein R. I., 2017, [MNRAS](#), **469**, 4370
- Zasov A. V., Saburova A. S., Egorov O. V., Afanasiev V. L., 2018, [MNRAS](#), **477**, 4908
- Zhang K., et al., 2017, [MNRAS](#), **466**, 3217
- van der Marel R. P., Franx M., 1993, [ApJ](#), **407**, 525